International Journal of Minerals, Metallurgy and Materials
Volume 28, Number 1, January 2021, Page 120
https://doi.org/10.1007/s12613-020-2159-0

Microstructure and mechanical properties of ultralow carbon high-strength steel weld metals with or without Cu−Nb addition

Xing-hai Yang[1)], *Xiao-hua Chen*[2)], *Shi-wei Pan*[2)], *Zi-dong Wang*[1)], *Kai-xuan Chen*[1)], *Da-yong Li*[3)], *and Jun-wei Qin*[1)]

1) School of Material Science and Engineering, University of Science and Technology Beijing, Beijing 100083, China
2) State Key Laboratory for Advanced Metals and Materials, University of Science and Technology Beijing, Beijing 100083, China
3) State Key Laboratory of Advanced Welding and Joining, Harbin Institute of Technology, Harbin 150001, China
(Received: 20 April 2020; revised: 5 August 2020; accepted: 6 August 2020)

Abstract: Two types of ultralow carbon steel weld metals (with and without added Cu−Nb) were prepared using gas metal arc welding (GMAW) to investigate the correlation between the microstructure and mechanical properties of weld metals. The results of microstructure characterization showed that the weld metal without Cu−Nb was mainly composed of acicular ferrite (AF), lath bainite (LB), and granular bainite (GB). In contrast, adding Cu−Nb to the weld metal caused an evident transformation of martensite and grain coarsening. Both weld metals had a high tensile strength (more than 950 MPa) and more than 17% elongation; however, their values of toughness deviated greatly, with a difference of approximately 40 J at −50°C. Analysis of the morphologies of the fracture surfaces and secondary cracks further revealed the correlation between the microstructure and mechanical properties. The effects of adding Cu and Nb on the microstructure and mechanical properties of the weld metal are discussed; the indication is that adding Cu−Nb increases the hardenability and grain size of the weld metal and thus deteriorates the toughness.

Keywords: weld metal; microstructure; mechanical properties; hardenability; grain coarsening

1. Introduction

Welding is the most essential joining technique used in industry, and it plays a significant role in determining the final performance of steel construction, especially when high-strength steel is used [1]. Much research has been conducted on the microstructure and mechanical properties of high-strength steel welded joints in the heat affected zone (HAZ) [2−4]. However, the comprehensive properties of a weld metal obtained by melting welding consumables also have a great influence on the overall high-strength steel welded structure. When conventional high-strength steels are welded, the mechanical properties of the welded joints are obviously lower because of their high carbon equivalent (CE), and this leads to various defects during welding, such as welding cracks [5]. Because the amount of carbon accounts for a high proportion of the CE in steels [6], reducing the carbon content is important for improving the weldability of steel [7]. Therefore, high-strength low alloy (HSLA) steels that contain less than 0.10wt% carbon have been designed and widely used in many industrial fields, such as shipbuilding and pressure vessel and pipeline construction [8−10], because of their good weldability.

The primary welding methods for HSLA steel are arc welding techniques, including gas metal arc welding (GMAW) and gas tungsten arc welding (GTAW) [11−12]. In these techniques, the design of the welding wire is crucial because it ensures a good match between the weld metal (WM) and base metal (BM) in terms of their mechanical properties. In previous studies [7,13−16], the carbon content of the welding wire used for high-strength steel was generally between 0.06wt%–0.10wt%, and the tensile strength of the weld metal was in the range of 700–950 MPa. However, hardening and brittle phases, such as martensite and martensite−austenite (M−A), are easily generated in the weld metal when it contains more than 0.05wt% carbon, and this causes the impact toughness to deteriorate. In this case, post-welding heat treatment (PWHT) must be implemented to improve the toughness of the weld metal, although it usually increases costs [14−15].

Corresponding authors: Xiao-hua Chen E-mail: chenxh@skl.ustb.edu.cn; Zi-dong Wang E-mail: wangzd@mater.ustb.edu.cn

For a high-strength steel weld metal, using an ultralow carbon (<0.03wt%) welding wire with microalloying elements may be a feasible way to obtain applicable mechanical properties. In previous studies, it was suggested that adding Cu to a weld metal can improve the strength as a result of the solid solution hardening effect [17], and that adding a small amount of Nb produces undissolved precipitates, which thereby refine the austenite grain size [18]. In this context, it is worth further investigating if adding a certain amount of Cu−Nb into an ultralow carbon welding wire results in beneficial effects in a weld metal.

In this paper, two types of ultralow carbon welding wires (one with and one without added Cu−Nb) were designed. Acceptable mechanical properties for weld metals without PWHT can be obtained using the two types of welding wire, and thus, the weldability of steels can also be improved. Meanwhile, with an ultralow carbon content level (<0.03wt%), the tensile strengths of the weld metals exceeded 950 MPa in this work, which were significantly higher than those reported previously for weld metals [7,13−16,19−20]. The effects that adding Cu−Nb have on the microstructure and mechanical properties of a weld metal are also discussed.

2. Experimental

2.1. Materials and welding procedures

10Ni5CrMoV HSLA steel plates with a thickness of 20 mm were selected as the BM [10]. For the BM, steel plates were first cut into two pieces using flame cutting, and then the edges were processed to form each piece into a trapezoidal groove via carbon arc air gouging. The angle between the groove bevel and vertical direction was 22.5°, as shown in Fig. 1(a). Two types of ultralow carbon steel welding wires, welding wire 1 (W1) and welding wire 2 (W2) (each with a diameter of 1.2 mm), were fabricated, and their chemical compositions are provided in Table 1. Notably, the ultralow carbon steel welding wire had a relatively low CE. The impurity elements in the welding wire mainly included H, O, N, S, and P, and the concentrations of these elements must be precisely controlled within the following specified ranges: [H] ≤ 3 ppm, [O] ≤ 30 ppm, [N] ≤ 30 ppm, [S] ≤ 10 ppm, [P] ≤ 10 ppm, and [H] + [O] + [N] + [S] + [P] ≤ 60 ppm.

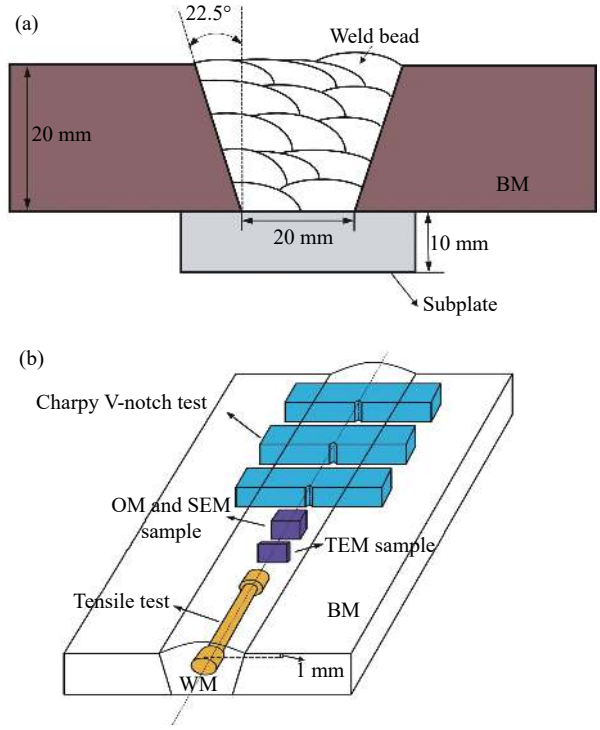

Fig. 1. (a) Weld groove size and multi-pass welding schematic diagram; (b) positions of specimens in the weld metal for microstructure analysis and mechanical tests.

The weld metal in a butt joint was prepared using GMAW at room temperature without PWHT, and 5vol% CO_2 and 95vol% Ar was selected to be the shielding gas. As shown in Fig. 1(a), a multi-pass welding process was used to feed the molten welding wire into the groove. The weld metals W1 and W2 (with a heat input of 10 kJ/cm) were labeled WM1 and WM2, respectively. The specific welding parameters of GMAW are presented in Table 2.

2.2. Microstructure characterization and mechanical tests

The specimens for optical microscopy (OM) and scanning electron microscopy (SEM) had the dimensions of

Table 1. Chemical compositions of welding wire 1 (W1) and welding wire 2 (W2) wt%

Welding wire	C	Si	Mn	Al	Ti	Cr	Ni	Cu	Nb	Mo	Fe	CE
W1	0.025	0.563	1.16	<0.06	<0.06	0.608	4.13	<0.01	<0.01	0.612	Bal.	0.37
W2	0.020	0.575	1.19			0.576	4.24	0.15	0.082	0.638		0.38

Note: $CE = W_C + f(C)\cdot[W_{Si}/24 + W_{Mn}/6 + W_{Cu}/15 + W_{Ni}/20 + (W_{Cr}+W_{Mo}+W_V+W_{Nb})/5 + 5W_B]$; $f(C) = 0.75 + 0.25\tanh[20(W_C - 0.12)]$; W_C, W_{Si}, W_{Mn}, W_{Cu}, W_{Ni}, W_{Cr}, W_{Mo}, W_V, W_{Nb}, and W_B are the contents (wt%) of elements C, Si, Mn, Cu, Ni, Cr, Mo, V, Nb, and B, respectively [6].

Table 2. GMAW butt welding parameters

Welding current / A	Arc voltage / V	Welding speed / (cm·min^{-1})	Gas flow rate / (L·min^{-1})	Interpass temperature / °C	Heat input / (kJ·cm^{-1})
200 ± 10	25 ± 2	30 ± 2	20 ± 1	100−150	10

10 mm × 10 mm × 10 mm (Fig. 1(b)). The specimens were mechanical ground, polished, and etched with 4vol% nitric acid alcohol for 10–15 s at room temperature. The microstructure was then observed using a 9XB-PC optical microscope and Zeiss Auriga scanning electron microscope equipped with an energy dispersive spectrometer (EDS). After mechanical lapping, metallographic specimens of the weld metal (with dimensions of 10 mm × 10 mm × 2 mm) were electropolished using a continuous-current plant with a solution of 10vol% $HClO_4$, and then electron backscattered diffraction (EBSD) was conducted. Transmission electron microscopy (TEM) samples (with dimensions of 10 mm × 10 mm × 0.3 mm) were extracted from the weld seam and mechanically ground to foils that had a thickness of 50–60 μm. Disks of 3 mm in diameter were punched from the foils and then electropolished in a twin-jet apparatus with a solution of 10vol% $HClO_4$ at −20°C to further thin them to a thickness of less than 100 nm. TEM was conducted with an FEI TecnaiF30 operated at a voltage of 300 kV.

As shown in Fig. 1(b), rod-like tensile samples (dimensions: ϕ5 mm × 60 mm) with a gauge length of 30 mm as well as standard Charpy V-notch impact specimens (dimensions: 10 mm × 10 mm × 55 mm) were taken 1 mm below the upper surface of the BM along the welding direction, according to ISO 5178:2019 and ISO 9016:2012. Tensile tests were conducted in accordance with ISO 6892-1:2016 at room temperature using a WDW-200D electronic universal testing machine. For each weld metal, three Charpy V-notch impact specimens were tested on a ZBC2452-B pendulum impact test machine, according to ISO 148-1:2016. SEM was used to observe the morphologies of the fracture surface and secondary cracks beneath the impact fracture surface.

3. Results

3.1. Microstructure of weld metals

Fig. 2 shows the microstructure of WM1 and WM2 observed using OM. Each microstructure had a prior austenite grain boundary (PAGB). The microstructure of WM1 mainly consisted of acicular ferrite (AF), lath bainite (LB), and lath martensite (LM). In contrast, WM2 was predominantly a lath structure. Moreover, WM2 had a larger grain size than WM1 overall, which was embodied in the lath structure size and prior austenite grain size.

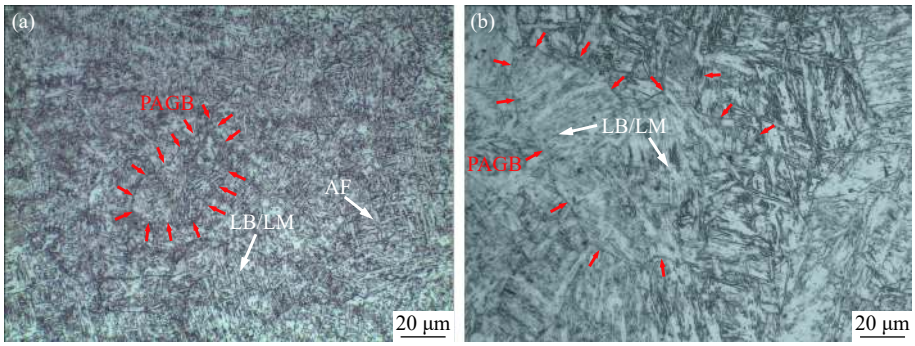

Fig. 2. OM images of weld metals: (a) WM1; (b) WM2.

The SEM images of WM1 and WM2 are shown in Fig. 3. Fig. 3(a) shows that WM1 was composed of fine AF and multiple forms of bainite, including granular bainite (GB) and LB. In addition, fine-grained AF (approximately 1 μm wide and 3 μm long) was mainly nucleated on the oxide inclusion and grew radially, as indicated by the white circle in Fig. 3(b) [21]. The inset of Fig. 3(b) shows the EDS results of the inclusion; these results show that the inclusion was a complex oxide of Ti, Al, Mn, and Si. Meanwhile, Figs. 3(c) and 3(d) show that the microstructure of WM2 predominantly consisted of LM with coarsened laths, and that prior austenite grains were segmented by these lath blocks [2]. In addition, many slender M−A constituents were present that had a high aspect ratio, and these constituents were distributed between the lath boundaries, as seen in Fig. 3(d).

The average prior austenite grain size (PAGS) and the area fraction of the main phases in the weld metals were measured using Image J software, and the results are provided in Table 3. LB and GB are classified as bainitic ferrite (BF) because they have the same transformation mechanism.

Table 3. Average PAGSs and phase area fractions of the weld metals

WM	PAGS / μm	Phase area fraction / %		
		AF	BF	Martensite
WM1	50.1 ± 2.4	20.5	72.7	6.8
WM2	91.4 ± 4.0	4.2	19.5	76.3

TEM was used to further investigate the typical morphologies of the lath structure in WM1 and WM2, and the results are shown in Fig. 4. In Fig. 4(a), LB in WM1 was composed of fine parallel ferrites that had an average length of less than 2 μm. The selected area electron diffraction (SAED) pattern in Fig. 4(b) reveals that there were retained austenite

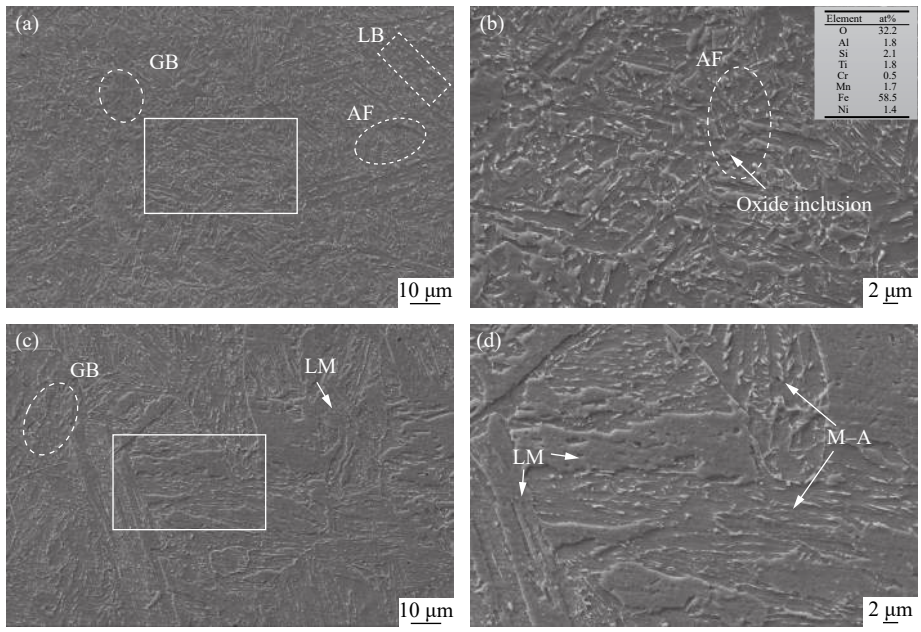

Fig. 3. SEM images of weld metals: (a, b) WM1; (c, d) WM2. (b) and (d) are the magnified views of local zones (indicated by the rectangles marked in solid white lines) in (a) and (c), respectively.

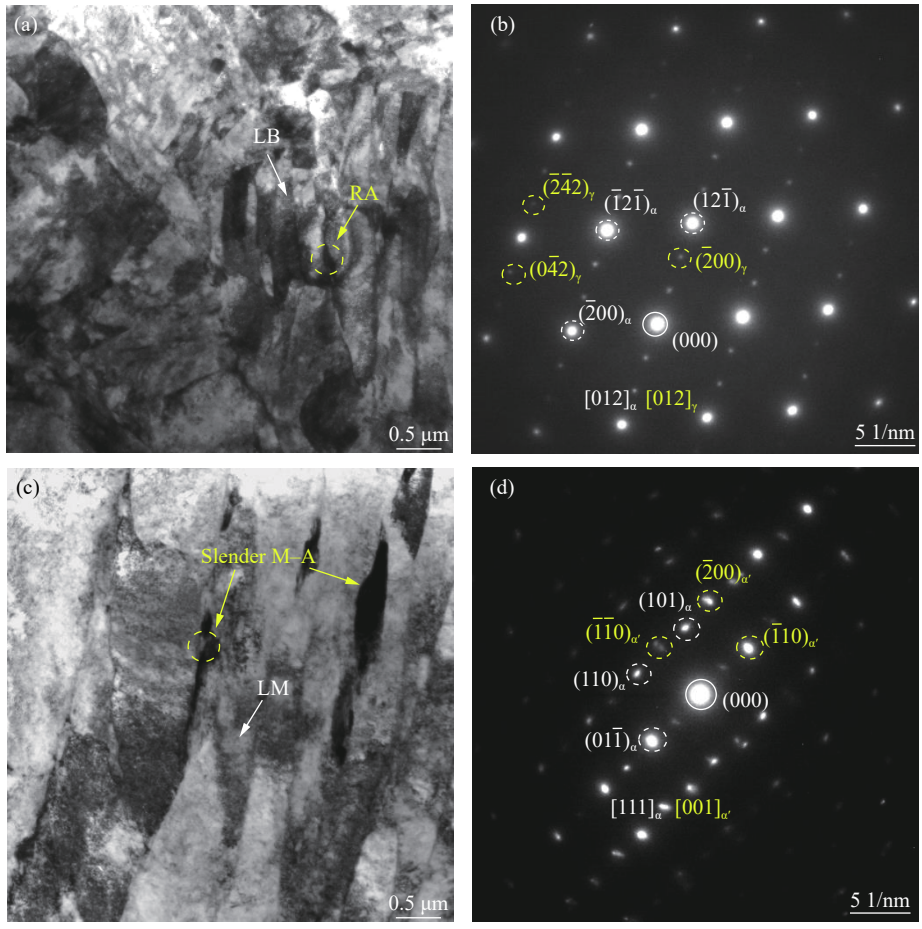

Fig. 4. Bright-field TEM micrographs for the weld metals: (a) WM1; (c) WM2. (b) and (d) show the corresponding SAED patterns of the regions indicated by dotted yellow circles in (a) and (c), respectively (α—Ferrite; γ—Austenite; α′—Martensite).

(RA) films distributed at the boundaries of LB. WM2 had an LM lath structure, and its lath was wider than that of WM1, as seen in Fig. 4(c). In addition, the SAED pattern in Fig. 4(d) for the slender M−A constituent shows that only martensite diffraction spots were present between laths, which reveals that the austenite in M−A was almost transformed into martensite. The presence of RA films rather than slender M−A constituents between laths is more conducive to improving the toughness of the weld metal [22].

The EBSD inverse pole figure (IPF) maps of WM1 and WM2 are presented in Figs. 5(a) and 5(b), respectively. The color legend for the IPF maps is shown in the bottom left corner of Fig. 5(a). The boundaries, including high-angle grain boundaries (HAGBs, >15°) and low-angle grain boundaries (LAGBs, 2°−15°), are coded by black and white lines, respectively. The low-angle boundaries consist of substructures, such as dislocations or lath boundaries of LB/LM [23]. For WM1 (Fig. 5(a)), the orientation colors of AF were separated from each other, which indicates that neighboring AF laths had different orientations and therefore made the orientation distribution homogeneous. In contrast, the grains in WM2 (Fig. 5(b)) exhibited a less diverse crystallographic

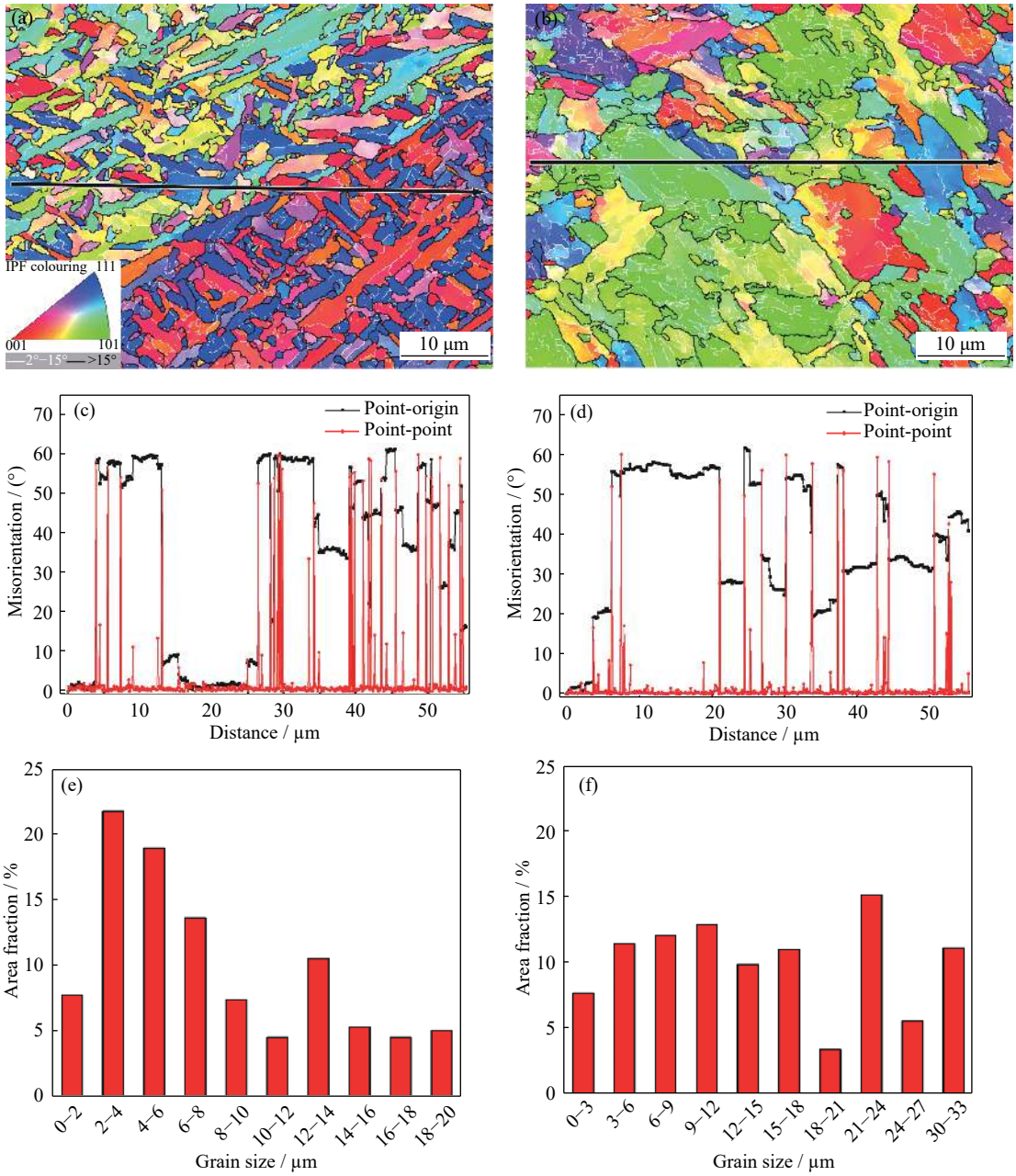

Fig. 5. EBSD IPF maps of (a) WM1 and (b) WM2; misorientation distributions of (c) WM1 and (d) WM2 along the linear paths indicated in (a) and (b), respectively; effective grain size distributions of (e) WM1 and (f) WM2.

orientation, and large-sized LM (with the same orientation) was dominant in the IPF maps. The misorientation angles along the path indicated by the black lines in Figs. 5(a) and 5(b) are shown in Figs. 5(c) and 5(d), respectively. Obviously, for WM1, the path crossed finer grains, whereas for WM2, the path crossed coarser grains. The red point-point misorientation values demonstrate that all HAGBs in the two weld metals had misorientation angles that were basically in the range of 50°−60°. In addition, a few boundaries (10°−20°) and a myriad of low misorientation angles (<5°) were distributed between HAGBs; these observations reflect a high density of substructures and dislocations in the grains. From three sets of EBSD data, quantified analyses of the grain size distributions of the weld metals were conducted. The results presented in Figs. 5(e) and 5(f) show that WM2 had much larger grains than WM1. The statistical results shown in Figs. 5(c) and 5(d) demonstrate that the amount of HAGB in WM1 was larger than that in WM2, which was consistent with the grain size distribution.

3.2. Mechanical properties of weld metals

The engineering stress−strain curves of the weld metals are presented in Fig. 6(a). The tensile test data are summarized at Table 4. The weld metals for the two types of welding wires both had a high tensile strength (above 950 MPa) and favorable elongation (over 17%). These values are rare for a welding wire with less than 0.03wt% carbon. Moreover, sample WM2 had a slightly higher strength than WM1, and this was more evident in terms of the yield strength. Fig. 6(b) shows histograms of the impact absorbed energies of the weld metals at −50°C. The average impact absorbed energy for WM1 could reach 50 J, whereas that for WM2 was slightly over 10 J. This result implies that the high yield strength of WM2 is at the expense of its impact toughness.

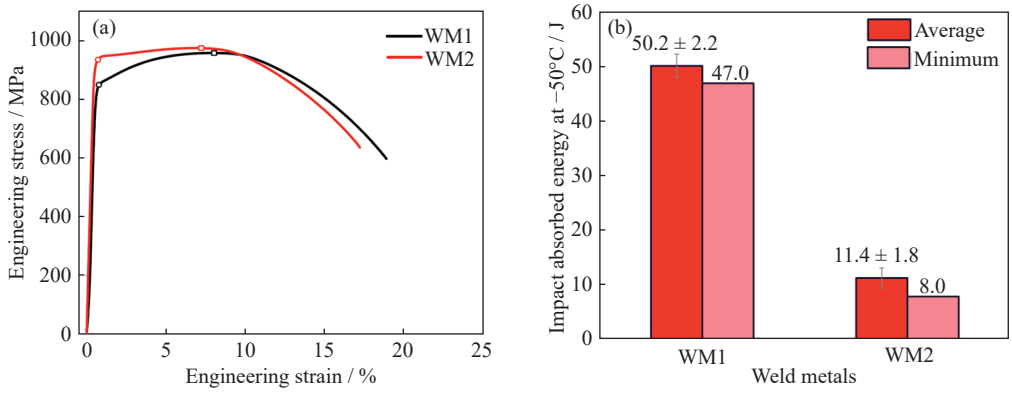

Fig. 6. (a) Engineering stress−strain curves of the weld metals (□—Tensile strength; ○—0.2% off-set yield strength); (b) V-notch impact absorbed energies of the weld metals at −50°C.

Table 4. Tensile test results of the weld metals

WM	Tensile strength, R_m / MPa	0.2% off-set yield strength, $R_{p0.2}$ / MPa	Total elongation / %
WM1	957	842	18.8
WM2	974	930	17.2

3.3. Fracture characteristics of the weld metals

Fig. 7 shows SEM images of the tensile fracture surfaces of the weld metals. The fracture surface is mainly divided into three regions: the fibrous zone (FZ), radical zone (RZ), and shear lip zone (SL) [24]. Figs. 7(a) and 7(b) show that the macroscopic fracture surfaces of WM1 and WM2 had only a central FZ and a marginal SL with few characteristics of an RZ. These observations indicate that WM1 and WM2 have excellent ductility at room temperature. In the FZ, secondary cracks extended below the fracture surface, and WM2 apparently had more cracks than WM1. Enlarged FZ micrographs of WM1 and WM2 are shown in Figs. 7(c) and 7(d), respectively. The FZ in WM1 had a few cleavage facets but was mainly covered with dimples. In contrast, the cleavage facet in the FZ of WM2 was obviously larger than that in WM1 and had fewer dimples. Detailed morphologies of the SL in WM1 and WM2 are presented in Figs. 7(e) and 7(f), respectively. For WM1 and WM2, the SL was dominated by dimples, and some cleavage facets (including unit cleavage facets) were also observed in the SL of WM2. Notably, the dimples in the SL were generally shallower than those in the FZ, and some of them tended to transform into cleavage facets; these dimples are marked as degenerated dimples.

Macrofracture surfaces of V-notch impact specimens for WM1 and WM2 are presented in Figs. 8(a) and 8(b), respectively. Three zones were present: the plastic fracture zone (PFZ), cleavage fracture zone (CFZ), and SL. PFZs are indicated by white dashed lines in Figs. 8(a) and 8(b). Obviously, the PFZ of WM1 was wider than that of WM2, and this is due to the higher impact toughness. The PFZ of WM1 was predominantly fine dimples (Fig. 8(c)), whereas that of WM2 had hybrid microstructures of large-sized cleavage facets and dimples (Fig. 8(d)). Figs. 8(e) and 8(f) show enlarged images

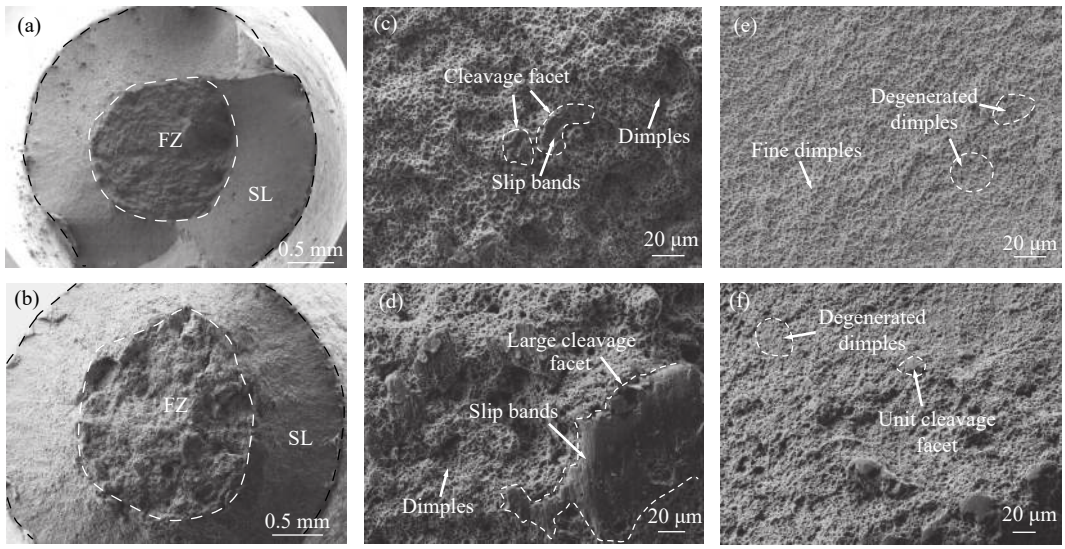

Fig. 7. SEM images of the tensile fracture surfaces of the weld metals: macrofracture surfaces of (a) WM1 and (b) WM2; enlarged micrographs of the FZs in (c) WM1 and (d) WM2; enlarged micrographs of the SLs in (e) WM1 and (f) WM2.

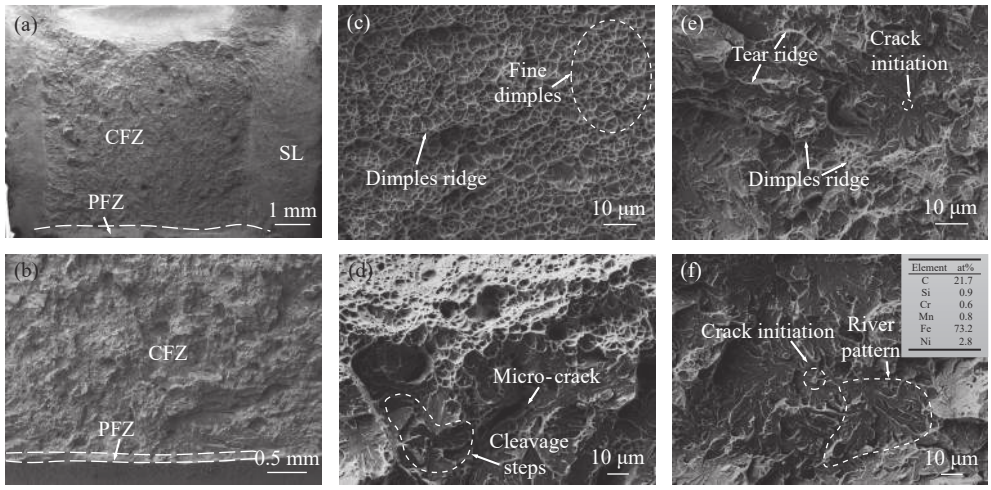

Fig. 8. SEM images of the impact fracture surfaces of the weld metals: macrofracture surfaces of (a) WM1 and (b) WM2; enlarged images of the PFZs in (c) WM1 and (d) WM2; enlarged images of the CFZs in (e) WM1 and (f) WM2. Inset in (f) shows EDS results of the M−A constituent enclosed by the dotted line.

of the CFZs, which consisted of cleavage facets and other cleavage patterns, that is, cleavage steps and river patterns. The CFZ of WM1 (Fig. 8(e)) contained cleavage facets separated by dimple ridges. The CFZ of WM2 contained cleavage facets and almost no dimples. Fig. 8(f) shows that a cleavage fracture in WM2 initiated from the blocky M−A constituent.

Fig. 9 shows the SEM morphologies of secondary cracks beneath the impact fracture surfaces. As seen in Figs. 9(a)–9(c), cracks were preferentially initiated on M−A constituents, which can be attributed to the debonding mechanism between M−A constituents and the matrix. In WM1, cracks were inclined to pass obliquely through the lath structure and to break the slender M−A constituents in the propagation path. Meanwhile, more crack deflections rather than crack arrests appeared at the grain boundaries in Fig. 9(d), which indicates that the microstructure of WM2 has poor resistance to crack propagation.

4. Discussion

4.1. Effect of adding Cu−Nb on the microstructure of the weld metals

Because the same welding procedure was used, the microstructure of the weld metal is primarily controlled by the chemical composition of the welding wire. At an ultralow carbon level, the weldability is improved, and the quantity of cementite and carbide in the weld metal is also reduced [25]. This result contributes significantly to limiting the decrease in toughness. In a previous study [20], the ultralow amount of

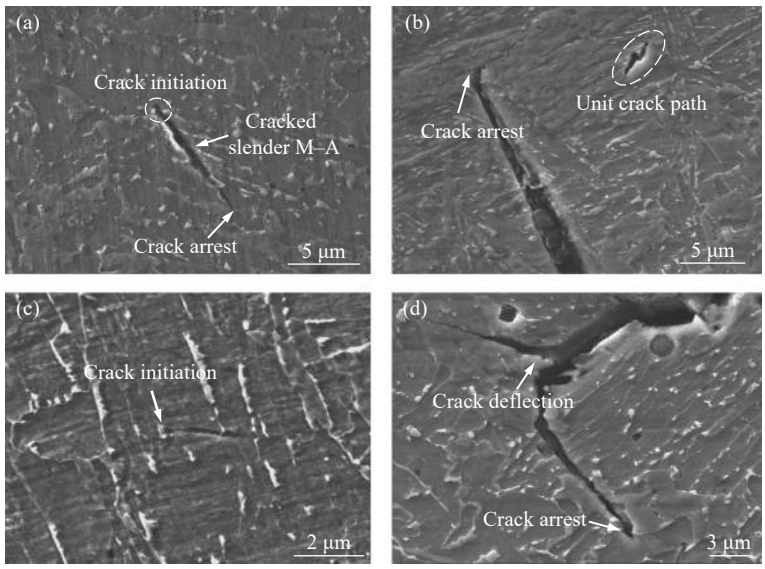

Fig. 9. SEM morphologies of secondary cracks in impact specimens of the weld metals: (a, b) WM1; (c, d) WM2.

carbon coupled with microalloys contributed to obtaining a fine bainitic structure in the weld metal, which had good comprehensive mechanical properties. The comparison of the chemical compositions in Table 1 shows that W2 contained additional amounts of Cu and Nb. Cu is mainly dissolved in austenite as a solid solution hardening element; this feature increases the stability of austenite and leads to an easier transformation of martensite and other low-temperature phases [24,26–27]. The addition of 0.18wt% Cu to the X120 steel welding wire has been found to increase the fraction of BF at the expense of GB in weld metal. In addition, the PAGS and ductile–brittle transition temperature of the weld metal increase with the addition of Cu, resulting in the deteriorated toughness [24]. Research on a low alloy steel weld metal [26] found that an increase in Cu simultaneously increases the hardness and tensile strength because of the solid solution hardening effect. As indicated in Table 3, the amount of martensite in WM2 reached 76%, whereas the amount of AF decreased to 4.2%. This observation reveals that the phase of WM2 is inclined to transform at low temperature, which reflects its strong hardenability. In contrast, WM1 was composed of phases, such as AF, GB, and LB that transform at a relatively high temperature. From the above discussion, it can be inferred that adding 0.15wt% Cu to W2 enhances the hardenability and induces more low-temperature transformation microstructures in WM2.

Generally, adding a trace amount of Nb to steel produces undissolved precipitates (typically, Nb(C, N)) that significantly improve the refinement of the austenite grain size [18,28]. However, compared to WM1, the grain size of WM2 increased remarkably when 0.08wt% Nb was added to W2, as indicated in Figs. 5(e) and 5(f). These observations imply that adding Nb does not cause grain refinement of WM2. Moon *et al.* [29] investigated the influence of adding Nb on a Ti-containing steel weld HAZ. The results suggested that (Ti, Nb)(C, N) complex particles are produced instead of multiple particles of Ti(C, N) and Nb(C, N) when Nb is added to Ti-containing steel. (Ti, Nb)(C, N) particles grow more easily because they have weaker bonds than either single Ti–N or Ti–C. Consequently, the comprehensive pinning effect of precipitated particles in steel is restrained, which leads to an increase in the size of austenite grains. In this study, W1 and W2 contained small amounts of Ti. Therefore, the refinement effect of Nb in WM2 is probably restricted because of a weaker pinning effect of (Ti, Nb)(C, N) complex particles. The PAGS of WM2 was larger than that of WM1, which also increases the degree of martensite transformation and the hardenability of WM2 [30].

4.2. Correlation between the microstructure and mechanical properties of the weld metals

Fig. 10 shows the true stress–strain curves of the weld metals and the corresponding strain hardening rate curves. According to the Hart criterion [31], under high uniaxial tensile stress, plastic elongation is easily affected by a local necking deformation, which leads to early failure of the tensile specimen. This relationship can be described by the inequality of the strain and strain hardening rate:

$$d\sigma/d\varepsilon + m\sigma < \sigma \quad (1)$$

where σ is the true stress, ε is the true strain, and m is the strain rate sensitivity, which can be negligible at room temperature [31]. The tensile specimen will enter the unstable necking stage when inequation (1) is established. Therefore, to prevent the tensile specimen from fracturing, the strain hardening rate ($d\sigma/d\varepsilon$) must be sufficiently high to change inequation (1). The intersection of the true stress–strain curve and the corresponding strain hardening rate curve ($d\sigma/d\varepsilon$ =

σ) is the critical condition for the tensile specimen to enter the necking stage. When $d\sigma/d\varepsilon < \sigma$, the strain hardening effect of the weld metal does not meet the requirement for a further increase in stress, and the fracture process for the tensile specimen begins. As seen in Fig. 10, a higher work-hardening rate was observed for WM1 than for WM2, and this causes the WM1 sample to have a higher ductility. With a decrease in the strain hardening rate, the WM1 sample, which had a higher $d\sigma/d\varepsilon$, can easily adapt to the increase in σ; this behavior effectively delays the necking process, which improves the ductility. Meanwhile, the lower yield strength of WM1 is also beneficial for improving the impact absorbed energy of this sample during the crack initiation stage.

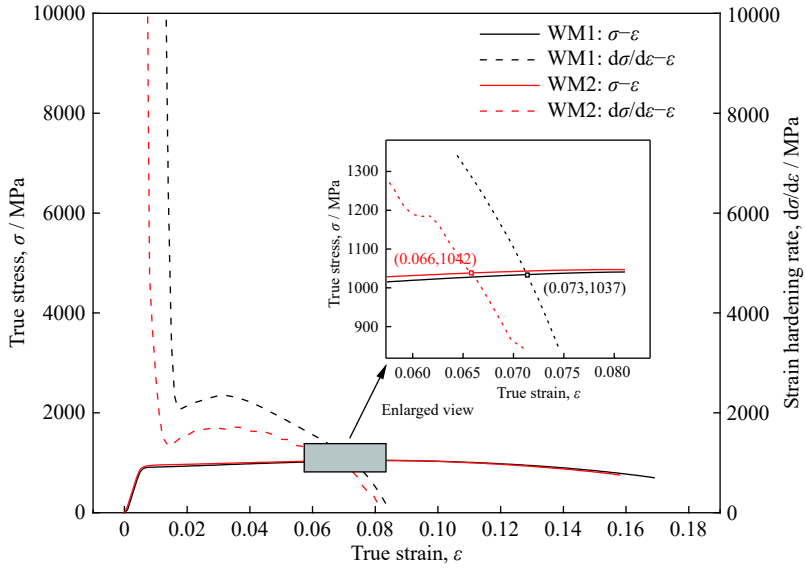

Fig. 10. True stress−true strain curves (solid lines) and strain hardening rate curves (dashed lines) of tensile specimens for the weld metals.

As seen from the tensile fracture surfaces shown in Figs. 7(c) and 7(d), many cleavage facets had parallel slip bands. The bands are formed via a mechanism of microvoid nucleation, growth, and polymerization [32]. Crack initiation of the cleavage facet usually results from a dislocation pile-up on slip bands. When shear stress is applied in a certain direction during the tensile process, small cleavage facets are likely to form via crack propagation. The larger size and higher quantity of cleavage facets in WM2 also demonstrate the poor ductility of WM2.

It is well known that AF, which has a fine grain size and cross-interlocking structure, is the desired microstructure of a weld metal in terms of improving toughness [21]. The radiating structure and HAGB of AF effectively restrain crack propagation. Moreover, grain size is one of the most important factors that affect impact toughness [33], and thus, grain coarsening of WM2 has an obvious deteriorating effect on impact toughness. Lan *et al.* [34] investigated the effect that refining prior austenite grains has on the coalescence of bainite; they reported that the combination of strength−ductility and toughness were significantly increased when the grain size was refined. Meanwhile, as seen from the IPF map of WM2 (Figs. 5(b) and 5(d)), the lath boundaries (indicated by the white solid line) are low misorientation angle (<15°) boundaries, which weakly impede crack propagation [23]. Therefore, the HAGB of WM2 has a relatively low density compared to that of WM1, which causes the CFZ to be completely covered with cleavage facets. As seen in Fig. 9, HAGB can induce deflection or arrest during crack propagation. This effect enhances the consumption of crack extension energy and improves the toughness. Because the amount of AF and fine grains is moderate, crack propagation in WM1 is easily arrested by HAGB. In contrast, cracks are easily propagated in WM2 because of the poor crack resistance of the coarsened LM. Hence, refining grain size to increase the density of HAGB is illustrated as an effective way to improve the toughness of the weld metal.

RA and M−A constituents are also important factors that affect the toughness of weld metals. The numerous mechanisms that support RA to improve the toughness of steel are as follows [35−36]:

(1) The deformation-induced martensite transformation (DIMT) from RA dissipates energy, which reduces the energy available for crack initiation and propagation.

(2) DIMT from RA delays the nucleation and coalescence of microvoids.

(3) RA without DIMT can be deformed, which blunts and arrests cracks.

On the other hand, the M−A constituent is most commonly a mixture of high carbon martensite plus RA [37]. The

hardness of the slender M–A constituent is higher than that of the ferrite matrix. This circumstance induces stress concentrations in the neighboring ferrite matrix, which is a key factor related to the fracture initiation and deterioration of toughness [38]. Wang *et al.* [15] showed that M–A constituents are the main nucleation sites for cracks in multi-pass weld metal. In our previous work [39], we investigated the effect that the morphology of M–A constituents has on impact toughness, and we found that M–A constituents with a slender shape contain almost complete martensite, which leads to lower toughness. The morphologies of the secondary cracks (Figs. 9(a) and 9(c)) indicate that the crack tends to propagate through the slender M–A constituent, which is also consistent with the findings of our previous work. Because of the enhanced hardenability of WM2, the martensite in the M–A constituent will be more completely transformed by inhibiting the carbon from diffusing into RA [35]. This behavior leaves a good deal of slender M–A without RA. Thus, the absence of RA between LM indicates that the degree of complete transformation of WM2 to the M–A constituent is higher than that of WM1, which causes the toughness loss of WM2 to be more severe.

5. Conclusions

(1) Two types of ultralow carbon weld metals were fabricated using GMAW. The weld metal without added Cu–Nb (WM1) had a high tensile strength of 957 MPa, a total elongation of 18.8%, and an average impact energy of 50.2 J at −50°C. The yield strength was increased by approximately 100 MPa in the weld metal with added Cu–Nb (WM2), whereas the impact toughness and strain hardening rate obviously decreased.

(2) WM1 was mainly composed of AF, GB, and LB, and the area fraction of AF was approximately 20%; this composition is beneficial for the ductility and toughness of WM1. In addition, WM2 was predominantly coarsened LM (area fraction of approximately 76%). The grain size (including PAGS) of WM2 was significantly larger than that of WM1, which causes the HAGB to have a relatively small density.

(3) Slender M–A constituents were distributed between martensitic laths in WM2, and these were transformed into martensite, whereas some austenitic films were still retained between laths in WM1.

(4) In WM2, the strength increased, but the toughness decreased; these observations are attributed to the enhanced hardenability and grain coarsening in the weld metal, as induced by the addition of Cu–Nb.

Acknowledgements

This work was financially supported by the Fundamental Research Funds for the Central Universities (No. FRF-AT-19-002), the Domain Foundation of Equipment Advance Research of the 13th Five-year Plan (No. 61409220121), and the National Natural Science Foundation of China (No. 51971031).

References

[1] G.K. Ahiale and Y.J. Oh, Microstructure and fatigue performance of butt-welded joints in advanced high-strength steels, *Mater. Sci. Eng. A*, 597(2014), p. 342.

[2] H. Xie, L.X. Du, J. Hu, G.S. Sun, H.Y. Wu, and R.D.K. Misra, Effect of thermo-mechanical cycling on the microstructure and toughness in the weld CGHAZ of a novel high strength low carbon steel, *Mater. Sci. Eng. A*, 639(2015), p. 482.

[3] P.S. Zhou, B. Wang, L. Wang, Y.W. Hu, and L. Zhou, Effect of welding heat input on grain boundary evolution and toughness properties in CGHAZ of X90 pipeline steel, *Mater. Sci. Eng. A*, 722(2018), p. 112.

[4] S.G. Lee, D.H. Lee, S.S. Sohn, W.G. Kim, K.K. Um, K.S. Kim, and S. Lee, Effects of Ni and Mn addition on critical crack tip opening displacement (CTOD) of weld-simulated heat-affected zones of three high-strength low-alloy (HSLA) steels, *Mater. Sci. Eng. A*, 697(2017), p. 55.

[5] L. Cui, X.Q. Yang, D.P. Wang, J. Cao, and W. Xu, Experimental study of friction taper plug welding for low alloy structure steel: Welding process, *Mater. Des.*, 62(2014), p. 271.

[6] Ş. Talaş, The assessment of carbon equivalent formulas in predicting the properties of steel weld metals, *Mater. Des.*, 31(2010), No. 5, p. 2649.

[7] L.Y. Lan, C.L. Qiu, D.W. Zhao, X.H. Gao, and L.X. Du, Analysis of microstructural variation and mechanical behaviors in submerged arc welded joint of high strength low carbon bainitic steel, *Mater. Sci. Eng. A*, 558(2012), p. 592.

[8] A.A. Gorni and P.R. Mei, Austenite transformation and age hardening of HSLA-80 and ULCB steels, *J. Mater. Process. Technol.*, 155-156(2004), p. 1513.

[9] Q.M. Jiang, X.Q. Zhang, and L.Q. Chen, Weldability of 1000 MPa grade ultra-low carbon bainitic steel, *J. Iron Steel Res. Int.*, 23(2016), No. 7, p. 705.

[10] D.Y. Li, D.Q. Yang, G.J. Zhang, X.H. Chen, and X. Luo, Microstructure and mechanical properties of welding metal with high Cr–Ni austenite wire through Ar–He–N_2 gas metal arc welding, *J. Manuf. Processes*, 35(2018), p. 190.

[11] R. Pamnani, T. Jayakumar, M. Vasudevan, and T. Sakthivel, Investigations on the impact toughness of HSLA steel arc welded joints, *J. Manuf. Processes*, 21(2016), p. 75.

[12] M. Mirzaei, R.A. Jeshvaghani, A. Yazdipour, and K. Zangeneh-Madar, Study of welding velocity and pulse frequency on microstructure and mechanical properties of pulsed gas metal arc welded high strength low alloy steel, *Mater. Des.*, 51(2013), p. 709.

[13] Y. Peng, X.N. Peng, X.M. Zhang, Z.L. Tian, and T. Wang, Microstructure and mechanical properties of GMAW weld metal of 890 MPa class steel, *J. Iron Steel Res. Int.*, 21(2014), No. 5, p. 539.

[14] J.C.F. Jorge, J.L.D. Monteiro, A.J.D.C. Gomes, I.D.S. Bott, L.F.G.D. Souza, M.C. Mendes, and L.S. Araújo, Influence of welding procedure and PWHT on HSLA steel weld metals, *J. Mater. Res. Technol.*, 8(2019), No. 1, p. 561.

[15] X.L. Wang, X.M. Wang, C.J. Shang, and R.D.K. Misra, Characterization of the multi-pass weld metal and the impact of re-

tained austenite obtained through intercritical heat treatment on low temperature toughness, *Mater. Sci. Eng. A*, 649(2016), p. 282.
[16] E. Keehan, L. Karlsson, H.-O. Andrén, and H.K.D.H. Bhadeshia, Influence of carbon, manganese and nickel on microstructure and properties of strong steel weld metals: Part 3 − Increased strength resulting from carbon additions, *Sci. Technol. Weld. Joining*, 11(2006), No. 1, p. 19.
[17] M. Es-Souni, P.A. Beaven, and G.M. Evans, Microstructure of copper-bearing C–Mn weld metal: As-welded and stress-relieved states, *Mater. Sci. Eng. A*, 130(1990), No. 2, p. 173.
[18] A. Di Schino and P.E. Di Nunzio, Effect of Nb microalloying on the heat affected zone microstructure of girth welded joints, *Mater. Lett.*, 186(2017), p. 86.
[19] A.J.M. Gomes, J.C.F. Jorge, L.F.G. de Souza, and I.D.S. Bott, Influence of chemical composition and post welding heat treatment on the microstructure and mechanical properties of high strength steel weld metals, *Mater. Sci. Forum*, 758(2013), p. 21.
[20] Z.L. Tian, C.Y. Ma, C.H. He, and Y. Peng, Development of an ultra-low carbon high strength welding wire, *Mater. Sci. Forum*, 426-432(2003), p. 1451.
[21] X.L. Wan, H.H. Wang, L. Cheng, and K.M. Wu, The formation mechanisms of interlocked microstructures in low-carbon high-strength steel weld metals, *Mater. Charact.*, 67(2012), p. 41.
[22] S. Kumar and S.K. Nath, Effect of weld thermal cycles on microstructures and mechanical properties in simulated heat affected zone of a HY 85 Steel, *Trans. Indian Inst. Met.*, 70(2017), No. 1, p. 239.
[23] Y.Y. Wang, R. Kannan, and L.J. Li, Characterization of as-welded microstructure of heat-affected zone in modified 9Cr–1Mo–V–Nb steel weldment, *Mater. Charact.*, 118(2016), p. 225.
[24] R. Cao, Z.S. Chan, J.J. Yuan, C.Y. Han, Z.G. Xiao, X.B. Zhang, Y.J. Yan, and J.H. Chen, The effects of silicon and copper on microstructures, tensile and Charpy properties of weld metals by refined X120 wire, *Mater. Sci. Eng. A*, 718(2018), p. 350.
[25] J. Hu, L.X. Du, G.S. Sun, H. Xie, and R.D.K. Misra, The determining role of reversed austenite in enhancing toughness of a novel ultra-low carbon medium manganese high strength steel, *Scripta Mater.*, 104(2015), p. 87.
[26] M.H. Avazkonandeh-Gharavol, M. Haddad-Sabzevar, and A. Haerian, Effect of copper content on the microstructure and mechanical properties of multipass MMA, low alloy steel weld metal deposits, *Mater. Des.*, 30(2009), No. 6, p. 1902.
[27] S.Y. Shin, S.Y. Han, B. Hwang, C.G. Lee, and S. Lee, Effects of Cu and B addition on microstructure and mechanical properties of high strength bainitic steels, *Mater. Sci. Eng. A*, 517(2009), No. 1-2, p. 212.
[28] S.T. Wei, and S.P. Lu, Effects of multiple normalizing processes on the microstructure and mechanical properties of low carbon steel weld metal with and without Nb, *Mater. Des.*, 35(2012), p. 43.
[29] J. Moon, S. Kim, H. Jeong, J. Lee, and C. Lee, Influence of Nb addition on the particle coarsening and microstructure evolution in a Ti-containing steel weld HAZ, *Mater. Sci. Eng. A*, 454-455(2007), p. 648.
[30] H.T. Zhao and E.J. Palmiere, Effect of austenite grain size on acicular ferrite transformation in a HSLA steel, *Mater. Charact.*, 145(2018), p. 479.
[31] E. Ma and T. Zhu, Towards strength–ductility synergy through the design of heterogeneous nanostructures in metals, *Mater. Today*, 20(2017), No. 6, p. 323.
[32] M. Zhou, Y.H. Li, Q. Hu, X.F. Li, and J. Chen, Investigations on edge quality and its effect on tensile property and fracture patterns of QP980, *J. Manuf. Processes*, 37(2019), p. 509.
[33] M. Calcagnotto, D. Ponge, and D. Raabe, Effect of grain refinement to 1 μm on strength and toughness of dual-phase steels, *Mater. Sci. Eng. A*, 527(2010), No. 29-30, p. 7832.
[34] H.F. Lan, L.X. Du, Q. Li, C.L. Qiu, J.P. Li, and R.D.K. Misra, Improvement of strength−toughness combination in austempered low carbon bainitic steel: The key role of refining prior austenite grain size, *J. Alloys Compd.*, 710(2017), p. 702.
[35] Z.Q. Wang, X.L. Wang, Y.R. Nan, C.J. Shang, X.M. Wang, K. Liu, and B. Chen, Effect of Ni content on the microstructure and mechanical properties of weld metal with both-side submerged arc welding technique, *Mater. Charact.*, 138(2018), p. 67.
[36] H. Qiu, L.N. Wang, J.G. Qi, H. Zuo, and K. Hiraoka, Enhancement of fracture toughness of high-strength Cr–Ni weld metals by strain-induced martensite transformation, *Mater. Sci. Eng. A*, 579(2013), p. 71.
[37] P.W. Hsu, F.H. Kao, S.H. Wang, J.R. Yang, H.Y. Chang, Y.M. Wang, and Q.X. Lin, Twinned formation in weld metal of titanium bearing nano precipitated high strength steel, *Mater. Chem. Phys.*, 136(2012), No. 2-3, p. 1103.
[38] C.L. Davis and J.E. King, Cleavage initiation in the intercritically reheated coarsegrained heat-affected zone. Part I. Fractographic evidence, *Metall. Mater. Trans. A*, 25(1994), No. 3, p. 563.
[39] X. Luo, X.H. Chen, T. Wang, S.W. Pan, and Z.D. Wang, Effect of morphologies of martensite–austenite constituents on impact toughness in intercritically reheated coarse-grained heat-affected zone of HSLA steel, *Mater. Sci. Eng. A*, 710(2018), p. 192.